

# Structural and magnetic characterization of CeTa<sub>7</sub>O<sub>19</sub> and YbTa<sub>7</sub>O<sub>19</sub> with two-dimensional pseudospin-1/2 triangular lattice

Feihao Pan,<sup>1,2</sup> Songnan Sun,<sup>1,2</sup> Alexander I. Kolesnikov,<sup>3</sup> Matthew B. Stone,<sup>3</sup> Jiale Huang,<sup>1,2</sup> Daye Xu,<sup>1,2</sup> Chenglin Shang,<sup>1,2</sup> Bingxian Shi,<sup>1,2</sup> Xuejuan Gui,<sup>1,2</sup> Zhongcen Sun,<sup>1,2</sup> Jinchen Wang,<sup>1,2</sup> Juanjuan Liu,<sup>1,2</sup> Hongxia Zhang,<sup>1,2</sup> Zhengxin Liu,<sup>1,2</sup> and Peng Cheng<sup>1,2,\*</sup>

<sup>1</sup>Laboratory for Neutron Scattering and Beijing Key Laboratory of Optoelectronic Functional Materials and MicroNano Devices,

Department of Physics, Renmin University of China, Beijing 100872, China

<sup>2</sup>Key Laboratory of Quantum State Construction and Manipulation (Ministry of Education), Renmin University of China, Beijing, 100872, China

<sup>3</sup>Neutron Scattering Division, Oak Ridge National Laboratory, Oak Ridge, Tennessee 37831, USA

Triangular lattice antiferromagnets are prototypes for frustrated magnetism and may potentially realize novel quantum magnetic states such as a quantum spin liquid ground state. A recent work suggests NdTa<sub>7</sub>O<sub>19</sub> with rare-earth triangular lattice is a quantum spin liquid candidate and highlights the large family of rare-earth heptatantalates as a framework for quantum magnetism investigation. In this paper, we report the structural and magnetic characterization of CeTa<sub>7</sub>O<sub>19</sub> and YbTa<sub>7</sub>O<sub>19</sub>. Both compounds are isostructural to NdTa<sub>7</sub>O<sub>19</sub> with no detectable structural disorder. For CeTa<sub>7</sub>O<sub>19</sub>, the crystal field energy levels and parameters are determined by inelastic neutron scattering measurements. Based on the crystal field result, the magnetic susceptibility data could be well fitted and explained, which reveals that CeTa<sub>7</sub>O<sub>19</sub> is a highly anisotropic Ising triangular-lattice antiferromagnet ( $g_z/g_{xy}\sim 3$ ) with very weak exchange interaction ( $J\sim 0.22$  K). For YbTa<sub>7</sub>O<sub>19</sub>, millimeter sized single crystals could be grown. The anisotropic magnetization and electron spin resonance data show that YbTa<sub>7</sub>O<sub>19</sub> has a contrasting in-plane magnetic anisotropy with  $g_z/g_{xy}\sim 0.67$  similar as that of YbMgGaO<sub>4</sub>. The above results indicate that CeTa<sub>7</sub>O<sub>19</sub> and YbTa<sub>7</sub>O<sub>19</sub> with pseudospin-1/2 ground states might either be quantum spin liquid candidate materials or find applications in adiabatic demagnetization refrigeration due to the weak exchange interaction.

## INTRODUCTION

The geometrically frustrated triangular-lattice antiferromagnets (TLAF) that carry spin-1/2 have attracted great attentions in recent decades. Due to the spin frustration and strong quantum fluctuations, they may host the famous quantum spin liquid state (QSL)[1, 2]. QSLs feature long-range quantum entanglement and support fractionalized excitation. They are also an important material basis for the realization of topological quantum computation in the future. Besides, TLAFs are also proposed to host other exotic quantum states of matter, such as the spin supersolid which may generate a giant magnetocaloric effect and be quite useful in adiabatic demagnetization refrigeration[3, 4].

For Kramer rare-earth (RE) ions such as Ce, Nd and Yb, if they have a well separated ground-state doublet due to the crystal field effect, they can be viewed to carry an effective spin  $S=1/2$  at low temperatures. In recent years, RE-based TLAFs have become important resources in searching for QSL candidates. The well known examples include the YbMgGaO<sub>4</sub> and AYbX<sub>2</sub> (A=Cs,K,Na; X=S,O,Se) family of materials[5–16]. However, an unambiguous confirmation of a QSL in these TLAFs is still lacking. There are arguments that many experimental evidences for QSLs such as spin excitation continuum or lack of magnetic order at very low temperature could also be caused by spin glass or random

singlet phases[17, 18]. It has been known that sizeable structural disorder may induce mimicry of a QSL[19, 20]. Therefore searching for and characterizing more TLAFs without atomic-site disorder would help to clarify many on-going questions in this research field.

NdTa<sub>7</sub>O<sub>19</sub> is recently proposed as a QSL candidate[21]. In this compound, the Nd<sup>3+</sup> form a two-dimensional (2D) triangular lattice without structural disorder. Inelastic neutron scattering (INS) measurements on the crystal-electric-field (CEF) levels confirm its magnetic ground state is characterized by effective spin-1/2 degrees of freedom. Combined with magnetization, electron spin resonance (ESR) and muon spin relaxation spectroscopy results, NdTa<sub>7</sub>O<sub>19</sub> is identified as a rare example with both highly anisotropic Ising-like exchange interactions and QSL features. Thereafter, the synthesis and structure of RETa<sub>7</sub>O<sub>19</sub> (RE= Pr, Sm, Eu, Gd, Dy, Ho) with triangular lattice were reported[22]. However, there are still two possible members in this material family, namely CeTa<sub>7</sub>O<sub>19</sub> and YbTa<sub>7</sub>O<sub>19</sub>, whose structural and magnetic properties are still unknown.

Based on this motivation, we have successfully synthesized CeTa<sub>7</sub>O<sub>19</sub> and YbTa<sub>7</sub>O<sub>19</sub>. They are found to be isostructural to NdTa<sub>7</sub>O<sub>19</sub> with a disorder-free 2D triangular lattice. Magnetic susceptibility, inelastic neutron scattering and ESR measurements reveal that CeTa<sub>7</sub>O<sub>19</sub> has a strong Ising-like anisotropy with effective spin-1/2 while YbTa<sub>7</sub>O<sub>19</sub> exhibits an in-plane mag-

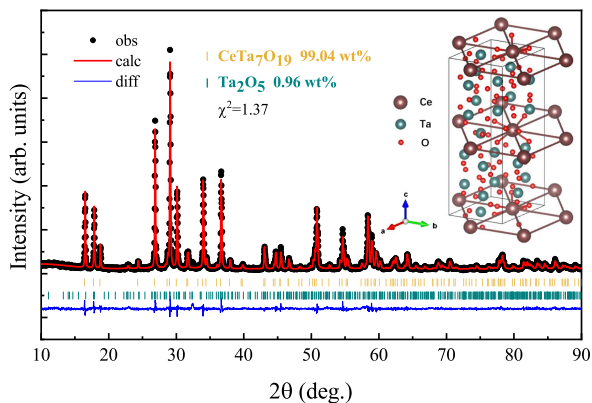


FIG. 1. X-ray diffraction patterns and Rietveld refinement on  $\text{CeTa}_7\text{O}_{19}$  powders. The inset shows the crystal structure of  $\text{CeTa}_7\text{O}_{19}$ .

netic anisotropy. Both  $\text{CeTa}_7\text{O}_{19}$  and  $\text{YbTa}_7\text{O}_{19}$  have very weak antiferromagnetic interactions, their magnetic properties are discussed with possible connections with a QSL ground state.

## METHODS

Polycrystalline  $\text{CeTa}_7\text{O}_{19}$  samples were prepared via the solid-state reaction method. Initially,  $\text{CeO}_2$  powder and  $\text{Ta}_2\text{O}_5$  powder were mixed in a ratio of 1:3.5, thoroughly ground and pressed into a pellet. Subsequently, the mixture was placed in an alumina crucible, heated at  $950^\circ\text{C}$  for 7 days in a muffle furnace and finally furnace cooled to room temperature. The product at this stage contains large amount of impurity phases. In order to get phase-pure  $\text{CeTa}_7\text{O}_{19}$  powder, the product was re-ground, pressed and heated at  $1000^\circ\text{C}$  in the furnace for 5 days. This procedure was repeated with the heating temperature increased by  $50^\circ\text{C}$  in each firing. Then after the final reaction at  $1150^\circ\text{C}$  for 5 days, nearly phase-pure  $\text{CeTa}_7\text{O}_{19}$  polycrystalline samples which exhibit a light yellow color could be obtained.

For the growth of  $\text{YbTa}_7\text{O}_{19}$  single crystals, firstly the precursor  $\text{YbOCl}$  powder needs to be prepared by the solid-state reaction of  $\text{NH}_4\text{Cl}$  and  $\text{Yb}_2\text{O}_3$  powder, similar as that in preparing  $\text{DyOCl}$  in our previous work[23]. Then  $\text{YbOCl}$ ,  $\text{Ta}_2\text{O}_5$ , and Ta were mixed in a molar ratio of 2:1:1, ground and pressed into pellet. The mixture was sealed in a quartz tube and evacuated to a high vacuum of  $5.0 \times 10^{-2}$  Pa. Subsequently, the quartz tube was heated to  $950^\circ\text{C}$  at a rate of  $50^\circ\text{C}/\text{h}$  and maintained at this temperature for 7 days. After furnace cooling to room temperature, the hexagonal plate-like  $\text{YbTa}_7\text{O}_{19}$  single crystals with dark brown color and typical dimensions of  $1.5 \times 1.5 \times 0.1 \text{ mm}^3$  could be found from the product.

We should mention that phase-pure polycrystalline

$\text{YbTa}_7\text{O}_{19}$  could not be obtained from direct solid-state reaction method. The impurity phases always exist with large volume fraction. Therefore the data on polycrystalline  $\text{YbTa}_7\text{O}_{19}$  were collected on powders crushed from single crystals. Alternatively, it is found that single crystals of  $\text{CeTa}_7\text{O}_{19}$  could not be grown using similar method described above.

X-ray diffraction (XRD) patterns of the samples were collected from a Bruker D8 Advance X-ray diffractometer using  $\text{Cu K}\alpha$  radiation. Magnetization measurements were carried out in Quantum Design MPMS3. Inelastic neutron scattering experiments were performed on the fine-resolution Fermi chopper spectrometer SEQUOIA at the Spallation Neutron Source of Oak Ridge National Laboratory and employed neutrons with incident energies ( $E_i$ ) of 140 meV[24, 25]. 4.6 g  $\text{CeTa}_7\text{O}_{19}$  and  $\text{LaTa}_7\text{O}_{19}$  powder samples were measured at 6.5 K. The data for non-magnetic analogue  $\text{LaTa}_7\text{O}_{19}$  served as background, which helps us to subtract phonon contributions from the measured spectra.

The ESR measurement of the powder sample was performed on the X-band ESR spectrometer (CIQTEK, EPR-100) with a dry cooling system. The spectra were recorded with the microwave power of 0.2 mW at the frequency of 9.77 GHz, modulation amplitude of 1 Gauss, time constant of 0.1 s.

## RESULTS AND DISCUSSIONS

### $\text{CeTa}_7\text{O}_{19}$

According to the current inorganic crystal structure database (ICSD),  $\text{CeTa}_7\text{O}_{19}$  forms a crystal structure with honeycomb lattice of Ce and there is no record for  $\text{YbTa}_7\text{O}_{19}$ . However, as shown in Fig. 1, the Rietveld refinement result on the powder XRD patterns of  $\text{CeTa}_7\text{O}_{19}$  reveals that it is isostructural to  $\text{NdTa}_7\text{O}_{19}$  with  $\text{Ce}^{3+}$  ions forming the 2D triangular lattice. The detailed crystallographic data are shown in the Supplemental Material[26]. There is some slight  $\text{Ta}_2\text{O}_5$  impurity identified from XRD which would not affect the following physical properties measurements. Within the  $ab$ -plane, the nearest Ce-Ce distance is 6.230 Å. This value is close to the nearest Nd-Nd distance 6.224 Å in  $\text{NdTa}_7\text{O}_{19}$ [21].

Fig. 2(a) presents the magnetic susceptibility  $\chi(T)$  data of  $\text{CeTa}_7\text{O}_{19}$ . Both the zero-field-cooling and field-cooling data overlaps well and show no signs of any magnetic order down to 1.8 K. From the temperature-dependent inverse susceptibility shown in Fig. 2(c), the data at above 120 K have linear temperature dependence which means that it could be well fitted by the Curie-Weiss (CW) model. The CW fit gives very large values of CW temperature  $\theta_{CW}$  and effective moment  $\mu_{eff}$  which should be notably affected by the crystal field excitation. Below 120 K, the  $1/\chi(T)$  data gradually deviate from the

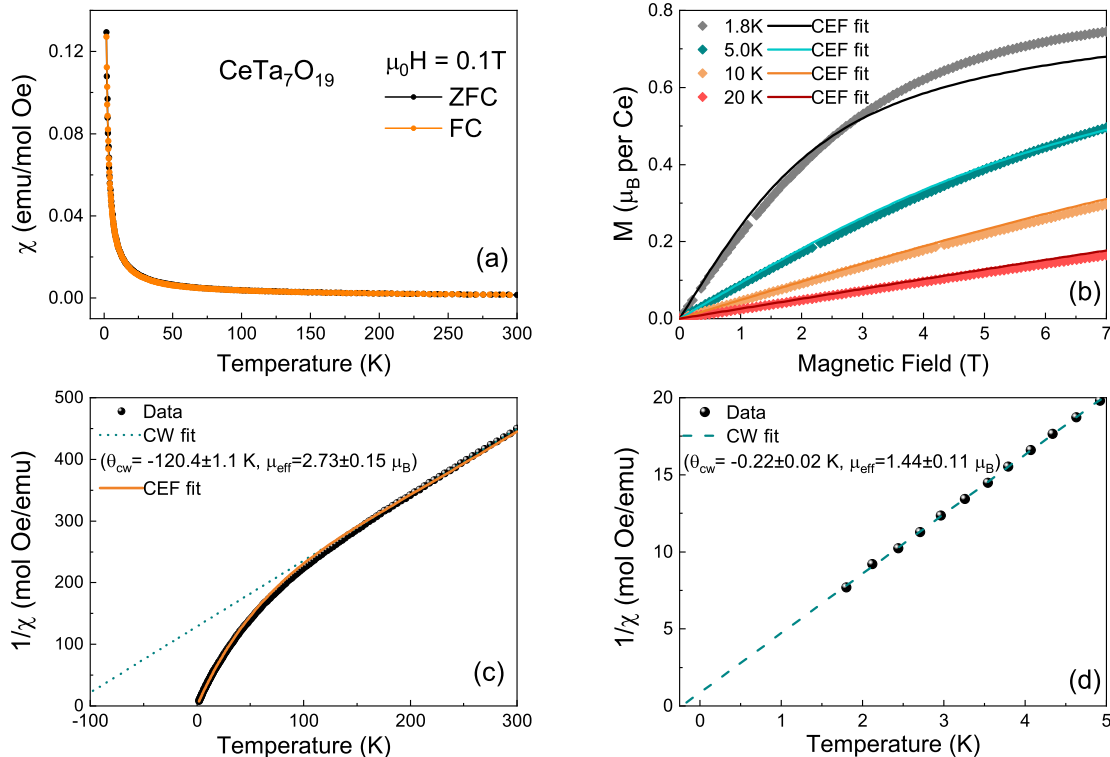


FIG. 2. (a) Temperature-dependent magnetic susceptibility  $\chi(T)$  of  $\text{CeTa}_7\text{O}_{19}$ . (b) Isothermal magnetization  $M(T)$  of  $\text{CeTa}_7\text{O}_{19}$  at selected temperatures and the solid lines are corresponding calculated result based on the crystal field parameters obtained from neutron scattering. (c) The Curie-Weiss fit on the high temperature susceptibility data (dotted line) and the crystal field model fit of the susceptibility data (solid line). (d) The Curie-Weiss fit on the susceptibility data below 5 K.

linear temperature dependence. However an additional CW behavior restores below 5 K as shown in Fig. 2(d) and the fit yields  $\theta_{CW} = -0.22 \pm 0.02$  K and  $\mu_{eff} = 1.44 \pm 0.11 \mu_B$ . For rare-earth compounds with very weak exchange interaction, such low temperature range is usually far above exchange coupling and far below the first CEF excitation. Therefore the CW fitting results on this range may reflect the strength of antiferromagnetic interaction and the pseudospin-1/2 state in  $\text{CeTa}_7\text{O}_{19}$ , as in the case of  $\text{NdTa}_7\text{O}_{19}$ [21] and  $\text{Ce}_2\text{Zr}_2\text{O}_7$ [27]. We will make further discussions after considering the following crystal field results.

For rare-earth compounds, the experimental determination of CEF levels and parameters is important to understand their magnetism. For  $\text{CeTa}_7\text{O}_{19}$ ,  $\text{Ce}^{3+}$  with  $J=5/2$  has an odd number of  $f$  electrons and the CEF potential from oxygen will split them into three Kramers doublets. Therefore at low temperature, two CEF excitations from the ground state to the two excited states are expected to be observed in the inelastic neutron scattering (INS) data. From the INS spectra of  $\text{CeTa}_7\text{O}_{19}$  at 6.5 K in Fig. 3(a), these two excitations can be identified at low- $Q$  range while the lattice (phonon) excitations dominate in the high- $Q$  range. After subtracting the spectra of the non-magnetic analogue  $\text{LaTa}_7\text{O}_{19}$ , two

flat CEF excitation bands are clearly observed as shown in Fig. 3(b). It is known that the CEF excitations are not coupled to propagating modes and do not possess a characteristic dispersion. Their scattering intensities decrease with  $Q$  following the magnetic form factor  $F(Q)^2$ , which is consistent with experimental result shown in the inset of Fig. 3(c). In Fig. 3(c), the fit on the data summed over  $2.5 \text{ \AA}^{-1} \leq Q \leq 4.5 \text{ \AA}^{-1}$  could confirm the energy of two CEF excitations are located at 42.9 meV and 67.1 meV. Therefore the schematic diagram of the CEF energy levels in  $\text{CeTa}_7\text{O}_{19}$  is presented in Fig. 3(d).

The CEF parameters could also be obtained through the fit of INS data. For  $\text{CeTa}_7\text{O}_{19}$ , the  $\text{Ce}^{3+}$  has a  $D_{3v}$  local point-group symmetry. Then the CEF Hamiltonian can be written as  $H_{CEF} = B_2^0 \hat{O}_2^0 + B_4^0 \hat{O}_4^0 + B_4^3 \hat{O}_4^3 + B_6^0 \hat{O}_6^0 + B_6^3 \hat{O}_6^3 + B_6^6 \hat{O}_6^6$ , where the  $B_l^m$  are the CEF parameters and the  $\hat{O}_l^m$  are the CEF Stevens equivalent operators. Since  $\text{Ce}^{3+}$  has  $J=5/2$  and all the sixth-order terms are zero, only three CEF parameters need to be derived from the fit of INS spectra. Using Mantid software[28], the best fit achieves with  $B_2^0 = -1.309$ ,  $B_4^0 = -0.020$  and  $B_4^3 = 3.335$  (unit: meV). Then the eigenstates of the CEF Hamiltonian could be calculated and shown in Table.I in the  $|m_J\rangle$  basis.

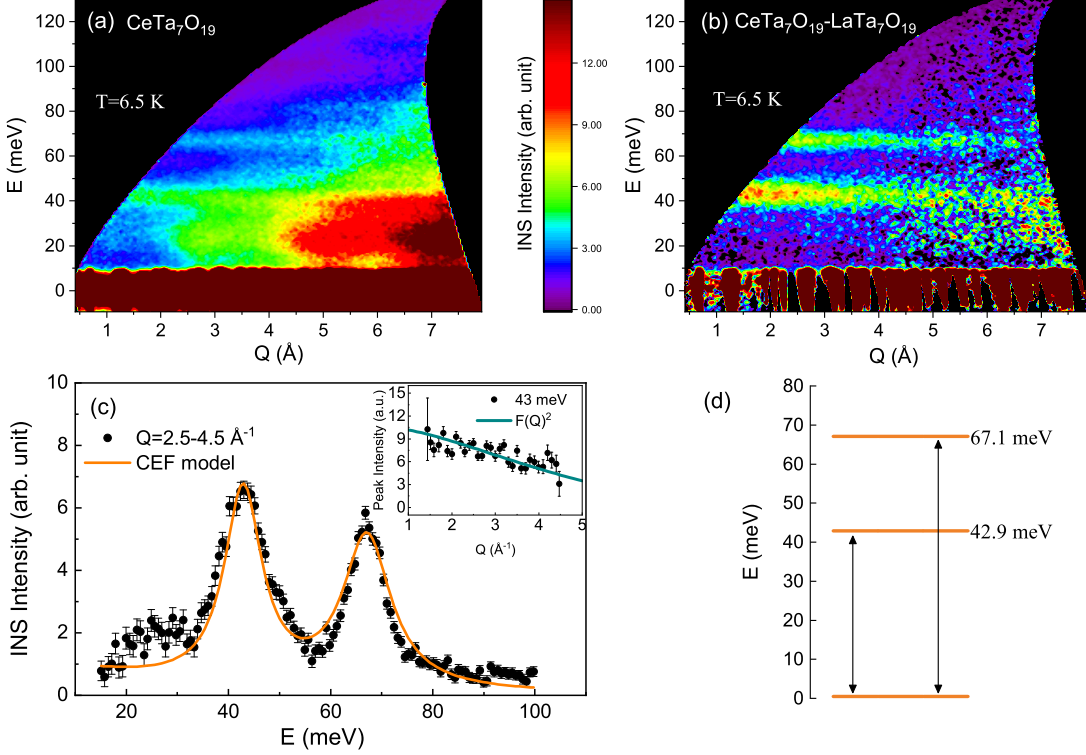


FIG. 3. (a) INS spectra from  $\text{CeTa}_7\text{O}_{19}$  powder sample with an incident neutron energy  $E_i=140$  meV. (b) INS spectrum after subtracting phonon contributions and other background scattering by measuring non-magnetic analogue  $\text{LaTa}_7\text{O}_{19}$ . (c) Energy spectrum obtained by integrating the INS data in (b) over the ranges  $2.5$ – $4.5$   $\text{\AA}^{-1}$ . The solid line is the CEF model fit and the inset shows the  $Q$ -dependent intensity of 43 meV peak agrees well with the magnetic form factor. (d) A scheme of the CEF splitting of the  $\text{Ce}^{3+}$  ground multiplet is shown.

$ \pm m_J\rangle$	$\pm\omega_0$	$\pm\omega_1$	$\pm\omega_2$
$ \pm 5/2\rangle$	0	0	0
$ \pm 3/2\rangle$	0	1	0
$ \pm 1/2\rangle$	$\pm 0.577$	0	0.817
$ \mp 1/2\rangle$	0	0	0
$ \mp 3/2\rangle$	0	0	0
$ \mp 5/2\rangle$	0.817	0	$\mp 0.577$
E(meV)	0	42.9	67.1

TABLE I. The CEF eigenstates wave functions given in the  $|\pm m_J\rangle$  basis and the corresponding energies of three  $\text{Ce}^{3+}$  doublets in  $\text{CeTa}_7\text{O}_{19}$ .

The CEF parameters determines the rare-earth single-ion magnetic anisotropy. For Ce-based magnetic materials, a large negative value of  $B_2^0$  for  $\text{CeTa}_7\text{O}_{19}$  usually leads to the easy  $c$ -axis magnetic anisotropy, while a positive  $B_2^0$  value indicates easy-plane magnetic anisotropy as in the case of Ce-based triangular antiferromagnets  $\text{CeCd}_3\text{As}_3$ [29] and  $\text{CePtAl}_4\text{Ge}_2$ [30]. Furthermore, the large  $B_4^3$  term implies a mixed ground state of  $|\pm 1/2\rangle$  and

$|\mp 5/2\rangle$ . A small value of  $B_4^0$  means the first excited CEF level would be a pure  $|\pm 3/2\rangle$  state. The expected consistent result has been demonstrated in  $\text{CeTa}_7\text{O}_{19}$  and  $\text{CeCd}_3\text{As}_3$ [29]. For  $\text{CePtAl}_4\text{Ge}_2$ [30], its near zero  $B_4^3$  term makes all CEF states being pure eigenstates. Meanwhile, the larger absolute value of  $B_2^0$  lead to the larger magnetic anisotropy. Based on the CEF parameters, the anisotropy ratio of magnetic susceptibility for  $\text{CeTa}_7\text{O}_{19}$  is  $\chi_c:\chi_{ab}\sim 8.56$  ( $T=1.8$  K) using PyCrystalField software [31].

From the above CEF results, several conclusions about the magnetism of  $\text{CeTa}_7\text{O}_{19}$  could be drawn. Firstly, the first excited CEF doublet lies at a very large energy gap 42.9 meV above the ground state, therefore  $\text{CeTa}_7\text{O}_{19}$  can be considered an effective spin-1/2 system below room temperature. Secondly, the negative second-order CEF parameter means that  $\text{CeTa}_7\text{O}_{19}$  possesses an easy-axis single-ion magnetic anisotropy along the  $c$ -axis. Thirdly, the knowledge on the CEF ground state allows us to determine the corresponding  $g$ -factor anisotropy using the equations below:



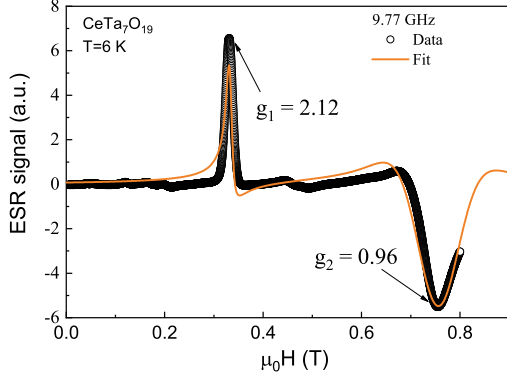


FIG. 4. The ESR spectrum measured at 9.77 GHz and 6 K on  $\text{CeTa}_7\text{O}_{19}$  powder samples. The solid line is the Lorentzian fit to the corresponding ESR signals.

$$\begin{aligned} g_z &= 2g_J |\langle \pm\omega_0 | J_z | \pm\omega_0 \rangle| = 2.57, \\ g_{xy} &= g_J |\langle \pm\omega_0 | J_{\pm} | \mp\omega_0 \rangle| = 0.86 \end{aligned} \quad (1)$$

where  $z$  and  $xy$  denote directions along the  $c$ -axis and parallel to the  $ab$ -plane, respectively.

We further performed the electron spin resonance (ESR) measurements on  $\text{CeTa}_7\text{O}_{19}$  to check the anisotropic  $g$ -factors. The well-resolved Ce ESR line is shown in Fig. 4. Through simulating the ESR spectra of  $\text{CeTa}_7\text{O}_{19}$  using EasySpin[32], an open-source MATLAB toolbox, two  $g$ -factor eigenvalues with  $g_1=2.12$  and  $g_2=0.96$  could be obtained. Considering the calculated  $g$ -factors from CEF analysis,  $g_1$  and  $g_2$  correspond well with  $g_z$  and  $g_{xy}$  respectively, since these values are in fairly agreement besides a maximum difference of 18% possibly caused by experimental errors.

The reliability of the CEF model obtained from the INS experiment could be further confirmed by simulating the magnetization data. As shown in Fig. 2(b) and (c), the simulated  $\chi(T)$  and  $M(H)$  curves based on non-interacting CEF model agree well with the experimental data. The deviation in the  $M(H)$  data at 1.8 K might be due to the exchange interaction which is not considered in the non-interacting CEF model. Furthermore, according to the  $g$ -factors obtained from CEF analysis, the  $g$ -factor of the powder sample should be  $g_{pwd.} = \sqrt{g_z^2/3 + 2g_{xy}^2/3} = 1.64$ . Then based on the corresponding effective spin  $J_{eff}=1/2$  model, the effective moment and saturation moment for  $\text{CeTa}_7\text{O}_{19}$  powder sample should be  $\mu_{eff} = \sqrt{J(J+1)}g_{pwd.}\mu_B = 1.42 \mu_B$  and  $\mu_{sat} = Jg_{pwd.}\mu_B = 0.82 \mu_B$ . These two values achieve a good agreement with the effective moment derived from the CW fit on the low temperature susceptibility data [inset of Fig. 2(d)] and the saturation moment deduced from  $M(H)$  data at 1.8 K [Fig. 2(b)]. This con-

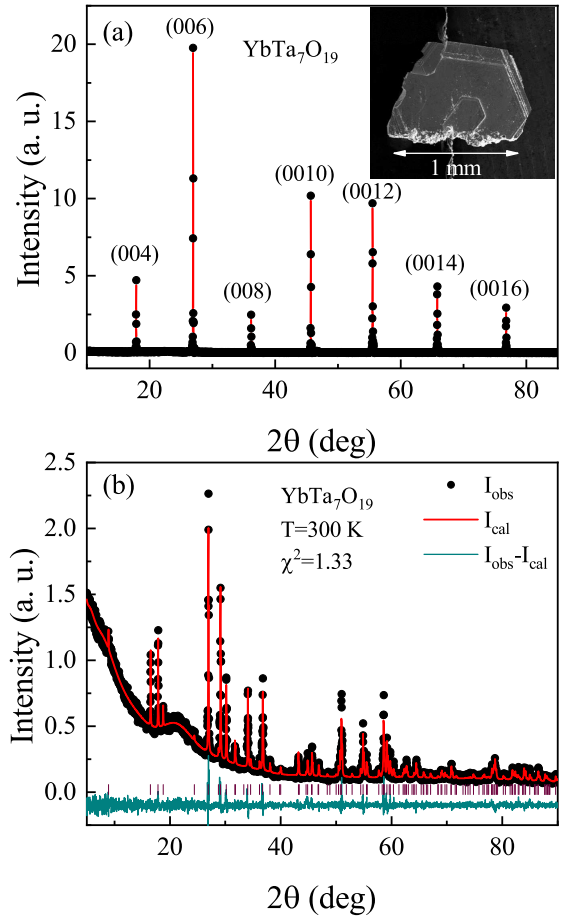


FIG. 5. (a) The XRD patterns from the  $ab$ -plane of a  $\text{YbTa}_7\text{O}_{19}$  single crystal. The inset shows a single crystal imaged by a scanning electron microscope. (b) XRD patterns of powders (crushed from single crystals) and the Rietveld refinement result.

sistency strongly suggests the CW temperature  $\theta_{CW} = 0.22$  K obtained from the low temperature CW fit could also be a good estimation on the strength of antiferromagnetic interaction in  $\text{CeTa}_7\text{O}_{19}$ . Future higher resolution lower energy inelastic neutron scattering measurements could be used to probe fluctuations at this energy scale.

Next, we could make a comparison of the magnetic properties between  $\text{CeTa}_7\text{O}_{19}$  and previously reported  $\text{NdTa}_7\text{O}_{19}$ . Firstly the two compounds have a similar Ising-like  $c$ -axis magnetic anisotropy. Then based on the  $g$ -factors from CEF analysis and using the same calculation method considering an Ising-like spin Hamiltonian as in the report of  $\text{NdTa}_7\text{O}_{19}$ [21], we could estimate the exchange anisotropy  $J_z/J_{xy} = g_z^2/g_{xy}^2 = 9$ , which is also highly anisotropic. Secondly, the estimated strength of antiferromagnetic exchange interaction in  $\text{CeTa}_7\text{O}_{19}$  is 0.22 K which is only half of that in  $\text{NdTa}_7\text{O}_{19}$  (0.46 K). Although the antiferromagnetic interaction is weak, theoretically, the perfect 2D triangular lattice and the ex-

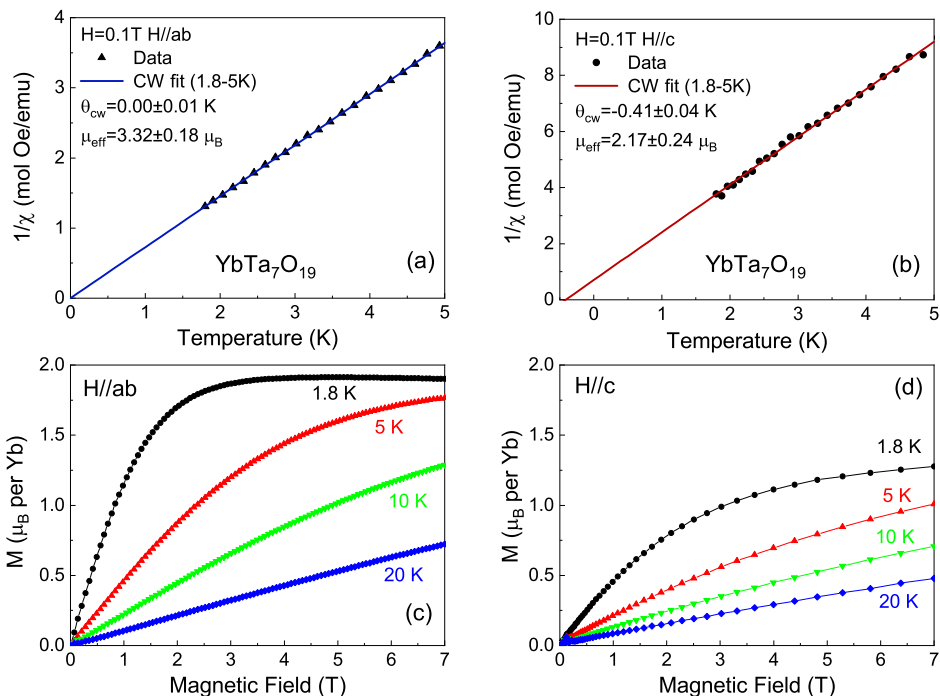


FIG. 6. (a) The CW fit result on the low temperature magnetic susceptibility data under  $H\parallel ab$ . Similar fit result along  $H\parallel c$  is shown in (b). (c,d) Isothermal magnetization along  $H\parallel ab$  and  $H\parallel c$  at selected temperatures.

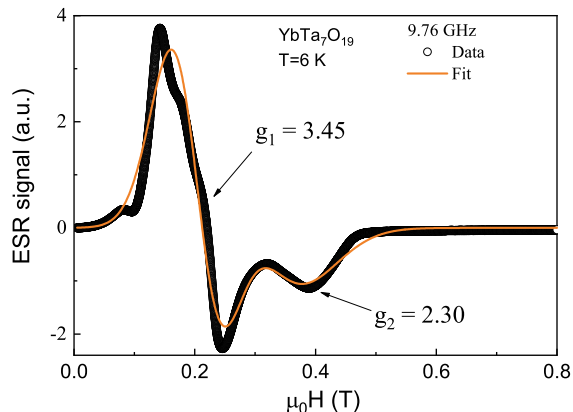


FIG. 7. The ESR spectrum measured at 9.76 GHz and 6 K on  $\text{YbTa}_7\text{O}_{19}$  powder samples. The solid line is the Lorentzian fit to the corresponding ESR signals.

change anisotropy close to the Ising limit in  $\text{CeTa}_7\text{O}_{19}$  may also potentially serve to realize a QSL state[33–36]. Further experimental characterization in ultra-low temperatures is needed for a final conclusion.

### $\text{YbTa}_7\text{O}_{19}$

Based on some early reports on the single crystal growth of  $\text{RETa}_7\text{O}_{19}$ [37–40], we managed to grow

$\text{YbTa}_7\text{O}_{19}$  single crystals with a modified condition as described in the METHODS section. As shown in the inset of Fig. 5(a), the single crystal of  $\text{YbTa}_7\text{O}_{19}$  has a hexagonal shape and a typical 2D layered feature. From both the XRD on the  $ab$ -plane and the powder XRD refinement on the powders which are crushed from single crystals,  $\text{YbTa}_7\text{O}_{19}$  could be confirmed to have the same crystal structure as  $\text{CeTa}_7\text{O}_{19}$ . The nearest Yb-Yb distance in the 2D triangular lattice is 6.202 Å. Detailed crystallographic data are presented in the Supplemental Material[26].

Next, we present the anisotropic magnetization data on the  $\text{YbTa}_7\text{O}_{19}$  single crystal in Fig. 6.  $\text{YbTa}_7\text{O}_{19}$  also does not show any sign of magnetic order down to 1.8 K. Similar as that of  $\text{CeTa}_7\text{O}_{19}$  and  $\text{NdTa}_7\text{O}_{19}$ , a CW behavior of magnetic susceptibility is re-established at low temperatures below 5 K. Therefore, we use the CW model to fit the low temperature susceptibility data and the results are contrasting for magnetic field along  $H\parallel ab$  ( $\theta_{CW}=0.0004$  K,  $\mu_{eff}=3.32\mu_B$ ) and  $H\parallel c$  ( $\theta_{CW}=-0.41$  K,  $\mu_{eff}=2.17\mu_B$ ), as shown in Fig. 6(a) and (b). Furthermore, the anisotropic isothermal magnetization data directly reveal that  $\text{YbTa}_7\text{O}_{19}$  has an easy  $ab$ -plane magnetic anisotropy with  $\mu_{sat}^{ab} \sim 1.91\mu_B$  and  $\mu_{sat}^c \sim 1.29\mu_B$  at 1.8 K, in contrast to  $c$ -axis anisotropy in  $\text{CeTa}_7\text{O}_{19}$  and  $\text{NdTa}_7\text{O}_{19}$ , but similar as the anisotropy in  $\text{YbMgGaO}_4$ [5]. Therefore a quantum XY-model may be expected for  $\text{YbTa}_7\text{O}_{19}$  at low temperatures and possibly a topological phase transition follow-

ing the so-called Berezinskii-Kosterlitz-Thouless scenario is also expected.

In order to obtain the anisotropic  $g$ -factors, the ESR measurement on  $\text{YbTa}_7\text{O}_{19}$  powder was performed and the result is presented in Fig. 7. From the same fitting method described above, two  $g$ -factors with  $g_1=3.45$  and  $g_2=2.30$  are derived. Based on the magnetic anisotropy determined from magnetization,  $g_1$  and  $g_2$  should be  $g_{xy}$  (parallel to the  $ab$ -plane) and  $g_z$  (perpendicular to the  $ab$ -plane) respectively. Since  $\text{Yb}^{3+}$  ion contains an odd number of electrons, the effective spin may also be described by a ground state Kramers doublet. Based on this pseudospin-1/2 assumption and the  $g$ -factors from ESR, we could calculate the effective and saturated moment for  $\text{YbTa}_7\text{O}_{19}$ . The results are  $\mu_{eff}^{ab}=2.99\mu_B$ ,  $\mu_{eff}^c=1.99\mu_B$ ,  $\mu_{sat}^{ab}=1.73\mu_B$  and  $\mu_{sat}^c=1.15\mu_B$ . These values are consistent with that obtained from magnetization data in Fig. 6, which suggests  $\text{YbTa}_7\text{O}_{19}$  can also be considered an effective spin-1/2 system.

In Fig. 6(b), the CW temperature  $\theta_{CW}=-0.41$  K by fitting  $\chi_c$  suggests  $\text{YbTa}_7\text{O}_{19}$  has an antiferromagnetic interaction strength comparable to  $\text{NdTa}_7\text{O}_{19}$ [21]. However, same fit on  $\chi_{ab}$  yields a near zero value. The measurement on another crystal exhibits roughly the same contrasting values. The interpretation on this result may need the determination of CEF parameters through INS experiment, which is currently unavailable due to the lack of large amount of phase-pure  $\text{YbTa}_7\text{O}_{19}$  powders. Additionally, the ESR line width of  $\text{YbTa}_7\text{O}_{19}$  ( $\sim 0.08$  T) at 6 K is comparable with that of triangular antiferromagnets  $\text{NaYbS}_2$ [41] and  $\text{KYbO}_2$ [42], but much larger than that of  $\text{CeTa}_7\text{O}_{19}$  ( $\sim 0.02$  T), which might suggest that the former compounds have stronger exchange interactions. However, there are many other factors which may broaden the ESR line width and not related to exchange interaction. Further ESR studies on the dilute magnetic doped crystal of  $\text{RETa}_7\text{O}_{19}$  may give deep insights on the exchange interaction in this family of materials[43].

## CONCLUSIONS

In summary, we have synthesized geometrically frustrated 2D TLAFs  $\text{CeTa}_7\text{O}_{19}$  and  $\text{YbTa}_7\text{O}_{19}$ . We find that these materials exhibit no structural disorder. For  $\text{CeTa}_7\text{O}_{19}$ , the CEF excitations and parameters are determined from INS experiment. Combined with the magnetic susceptibility analysis,  $\text{CeTa}_7\text{O}_{19}$  is identified as an effective spin-1/2 system with Ising-like magnetic anisotropy ( $g_z/g_{xy}\sim 3$ ) and weak antiferromagnetic exchange interaction ( $J\sim 0.22$  K). For  $\text{YbTa}_7\text{O}_{19}$ , its easy-plane magnetic anisotropy is directly identified by magnetization measurements on single crystal. Combined with ESR data analysis, the low temperature magnetic properties of  $\text{YbTa}_7\text{O}_{19}$  agree well with the expectation from a ground state Kramer doublet with effective spin-

1/2.

Although our initial structural and magnetic characterization of  $\text{CeTa}_7\text{O}_{19}$  and  $\text{YbTa}_7\text{O}_{19}$  shows that they could be considered as QSL candidate materials, it should be noted that their antiferromagnetic exchange interaction is much weaker than that of  $\text{YbMgGaO}_4$  and  $\text{AYbX}_2$ , which usually have  $J$  values of several kelvins. The reason should be the large distance between nearest RE-ions in the triangular lattice. As a result, it may be quite challenging for experimental characterizing the possible QSL state. On the other hand, the quite small  $J$  in  $\text{RETa}_7\text{O}_{19}$  means that their magnetic moments should be easily aligned by external magnetic field, causing a reduction of entropy. Therefore, both  $\text{CeTa}_7\text{O}_{19}$  and  $\text{YbTa}_7\text{O}_{19}$  could attract research interests as materials used in adiabatic demagnetization refrigeration[44].

## ACKNOWLEDGEMENT

This work was supported by the National Natural Science Foundation of China (No. 12074426, No. 12474148), the Fundamental Research Funds for the Central Universities, and the Research Funds of Renmin University of China (Grants No. 22XNKJ40). A portion of this research used resources at the Spallation Neutron Source, a DOE Office of Science User Facility operated by the Oak Ridge National Laboratory. The beam time was allocated to SEQUOIA spectrometer on proposal number IPTS-30317.1.

---

\* Corresponding author: [pcheng@ruc.edu.cn](mailto:pcheng@ruc.edu.cn)

- [1] Y. Zhou, K. Kanoda, and T.-K. Ng, Quantum spin liquid states, *Rev. Mod. Phys.* **89**, 025003 (2017).
- [2] C. Broholm, R. J. Cava, S. A. Kivelson, D. G. Nocera, M. R. Norman, and T. Senthil, Quantum spin liquids, *Science* **367**, eaay0668 (2020).
- [3] J. Xiang, C. Zhang, Y. Gao, W. Schmidt, K. Schmalzl, C.-W. Wang, B. Li, N. Xi, X.-Y. Liu, H. Jin, G. Li, J. Shen, Z. Chen, Y. Qi, Y. Wan, W. Jin, W. Li, P. Sun, and G. Su, Giant magnetocaloric effect in spin supersolid candidate  $\text{Na}_2\text{BaCo}(\text{PO}_4)_2$ , *Nature* **625**, 270 (2024).
- [4] J. Sheng, L. Wang, A. Candini, W. Jiang, L. Huang, B. Xi, J. Zhao, H. Ge, N. Zhao, Y. Fu, J. Ren, J. Yang, P. Miao, X. Tong, D. Yu, S. Wang, Q. Liu, M. Kofu, R. Mole, G. Biasiol, D. Yu, I. A. Zaliznyak, J.-W. Mei, and L. Wu, Two-dimensional quantum universality in the spin-1/2 triangular lattice quantum antiferromagnet  $\text{Na}_2\text{BaCo}(\text{PO}_4)_2$ , *Proc. Natl. Acad. Sci. U.S.A.* **119**, e2211193119 (2022).
- [5] Y. Li, G. Chen, W. Tong, L. Pi, J. Liu, Z. Yang, X. Wang, and Q. Zhang, Rare-Earth Triangular Lattice Spin Liquid: A Single-Crystal Study of  $\text{YbMgGaO}_4$ , *Phys. Rev. Lett.* **115**, 167203 (2015).
- [6] W. Liu, Z. Zhang, J. Ji, Y. Liu, J. Li, X. Wang, H. Lei, G. Chen, and Q. Zhang, Rare-Earth Chalcogenides: A

- Large Family of Triangular Lattice Spin Liquid Candidates, *Chinese Physics Letters* **35**, 117501 (2018).
- [7] K. M. Ranjith, D. Dmytriieva, S. Khim, J. Sichelschmidt, S. Luther, D. Ehlers, H. Yasuoka, J. Wosnitza, A. A. Tsirlin, H. Kühne, and M. Baenitz, Field-induced instability of the quantum spin liquid ground state in the  $J_{\text{eff}} = \frac{1}{2}$  triangular-lattice compound  $\text{NaYbO}_2$ , *Phys. Rev. B* **99**, 180401 (2019).
- [8] M. M. Bordelon, E. Kenney, C. Liu, T. Hogan, L. Posthuma, M. Kavand, Y. Lyu, M. Sherwin, N. P. Butch, C. Brown, M. J. Graf, L. Balents, and S. D. Wilson, Field-tunable quantum disordered ground state in the triangular-lattice antiferromagnet  $\text{NaYbO}_2$ , *Nature Physics* **15**, 1058 (2019).
- [9] L. Ding, P. Manuel, S. Bachus, F. Grubler, P. Gegenwart, J. Singleton, R. D. Johnson, H. C. Walker, D. T. Adroja, A. D. Hillier, and A. A. Tsirlin, Gapless spin-liquid state in the structurally disorder-free triangular antiferromagnet  $\text{NaYbO}_2$ , *Phys. Rev. B* **100**, 144432 (2019).
- [10] M. Baenitz, P. Schlender, J. Sichelschmidt, Y. A. Onykiienko, Z. Zangeneh, K. M. Ranjith, R. Sarkar, L. Hozoi, H. C. Walker, J.-C. Orain, H. Yasuoka, J. Van Den Brink, H. H. Klauss, D. S. Inosov, and T. Doert,  $\text{NaYbS}_2$ : A planar spin- $\frac{1}{2}$  triangular-lattice magnet and putative spin liquid, *Phys. Rev. B* **98**, 220409 (2018).
- [11] K. M. Ranjith, S. Luther, T. Reimann, B. Schmidt, P. Schlender, J. Sichelschmidt, H. Yasuoka, A. M. Strydom, Y. Skourski, J. Wosnitza, H. Kühne, T. Doert, and M. Baenitz, Anisotropic field-induced ordering in the triangular-lattice quantum spin liquid  $\text{NaYbSe}_2$ , *Phys. Rev. B* **100**, 224417 (2019).
- [12] Z. Zhang, X. Ma, J. Li, G. Wang, D. T. Adroja, T. P. Perring, W. Liu, F. Jin, J. Ji, Y. Wang, Y. Kamiya, X. Wang, J. Ma, and Q. Zhang, Crystalline electric field excitations in the quantum spin liquid candidate  $\text{NaYbSe}_2$ , *Phys. Rev. B* **103**, 035144 (2021).
- [13] Z. Zhang, J. Li, W. Liu, Z. Zhang, J. Ji, F. Jin, R. Chen, J. Wang, X. Wang, J. Ma, and Q. Zhang, Effective magnetic Hamiltonian at finite temperatures for rare-earth chalcogenides, *Phys. Rev. B* **103**, 184419 (2021).
- [14] P.-L. Dai, G. Zhang, Y. Xie, C. Duan, Y. Gao, Z. Zhu, E. Feng, Z. Tao, C.-L. Huang, H. Cao, A. Podlesnyak, G. E. Granroth, M. S. Everett, J. C. Neufeind, D. Voneshen, S. Wang, G. Tan, E. Morosan, X. Wang, H.-Q. Lin, L. Shu, G. Chen, Y. Guo, X. Lu, and P. Dai, Spinon Fermi Surface Spin Liquid in a Triangular Lattice Antiferromagnet  $\text{NaYbSe}_2$ , *Phys. Rev. X* **11**, 021044 (2021).
- [15] Z. Zhang, J. Li, M. Xie, W. Zhuo, D. T. Adroja, P. J. Baker, T. G. Perring, A. Zhang, F. Jin, J. Ji, X. Wang, J. Ma, and Q. Zhang, Low-energy spin dynamics of the quantum spin liquid candidate  $\text{NaYbSe}_2$ , *Phys. Rev. B* **106**, 085115 (2022).
- [16] J. Wu, J. Li, Z. Zhang, C. Liu, Y. H. Gao, E. Feng, G. Deng, Q. Ren, Z. Wang, R. Chen, J. Embs, F. Zhu, Q. Huang, Z. Xiang, L. Chen, Y. Wu, E. S. Choi, Z. Qu, L. Li, J. Wang, H. Zhou, Y. Su, X. Wang, G. Chen, Q. Zhang, and J. Ma, Magnetic field effects on the quantum spin liquid behaviors of  $\text{NaYbS}_2$ , *Quantum Frontiers* **1**, 13 (2022).
- [17] S. Zhang, H. J. Changlani, K. W. Plumb, O. Tchernyshyov, and R. Moessner, Dynamical Structure Factor of the Three-Dimensional Quantum Spin Liquid Candidate  $\text{NaCaNi}_2\text{F}_7$ , *Phys. Rev. Lett.* **122**, 167203 (2019).
- [18] Z. Zhu, P. A. Maksimov, S. R. White, and A. L. Chernyshev, Disorder-Induced Mimicry of a Spin Liquid in  $\text{YbMgGaO}_4$ , *Phys. Rev. Lett.* **119**, 157201 (2017).
- [19] I. Kimchi, A. Nahum, and T. Senthil, Valence Bonds in Random Quantum Magnets: Theory and Application to  $\text{YbMgGaO}_4$ , *Phys. Rev. X* **8**, 031028 (2018).
- [20] Z. Ma, J. Wang, Z.-Y. Dong, J. Zhang, S. Li, S.-H. Zheng, Y. Yu, W. Wang, L. Che, K. Ran, S. Bao, Z. Cai, P. Čermák, A. Schneidewind, S. Yano, J. S. Gardner, X. Lu, S.-L. Yu, J.-M. Liu, S. Li, J.-X. Li, and J. Wen, Spin-Glass Ground State in a Triangular-Lattice Compound  $\text{YbZnGaO}_4$ , *Phys. Rev. Lett.* **120**, 087201 (2018).
- [21] T. Arh, B. Sana, M. Pregelj, P. Khuntia, Z. Jagličić, M. D. Le, P. K. Biswas, P. Manuel, L. Mangin-Thro, A. Ozarowski, and A. Zorko, The Ising triangular-lattice antiferromagnet neodymium heptatantalate as a quantum spin liquid candidate, *Nature Materials* **21**, 416 (2022).
- [22] L. Wang, Z. Ouyang, T. Xiao, Z. Li, and Z. Tian, Synthesis, structure and magnetism of  $\text{RTa}_7\text{O}_{19}$  (R = Pr, Sm, Eu, Gd, Dy, Ho) with perfect triangular lattice, *Journal of Alloys and Compounds* **937**, 168390 (2023).
- [23] C. Tian, F. Pan, L. Wang, D. Ye, J. Sheng, J. Wang, J. Liu, J. Huang, H. Zhang, D. Xu, J. Qin, L. Hao, Y. Xia, H. Li, X. Tong, L. Wu, J.-H. Chen, S. Jia, P. Cheng, J. Yang, and Y. Zheng,  $\text{DyOCl}$ : A rare-earth based two-dimensional van der Waals material with strong magnetic anisotropy, *Phys. Rev. B* **104**, 214410 (2021).
- [24] G. E. Granroth, A. I. Kolesnikov, T. E. Sherline, J. P. Clancy, K. A. Ross, J. P. C. Ruff, B. D. Gaulin, and S. E. Nagler, SEQUOIA: A Newly Operating Chopper Spectrometer at the SNS, *Journal of Physics: Conference Series* **251**, 012058 (2010).
- [25] M. B. Stone, J. L. Niedziela, D. L. Abernathy, L. DeBeer-Schmitt, G. Ehlers, O. Garlea, G. E. Granroth, M. Graves-Brook, A. I. Kolesnikov, A. Podlesnyak, and B. Winn, A comparison of four direct geometry time-of-flight spectrometers at the Spallation Neutron Source, *Review of Scientific Instruments* **85**, 045113 (2014).
- [26] See Supplemental Material at [URL will be inserted by publisher] for the Rietveld refinement result of  $\text{CeTa}_7\text{O}_{19}$  and  $\text{YbTa}_7\text{O}_{19}$ .
- [27] B. Gao, T. Chen, D. W. Tam, C.-L. Huang, K. Sasmal, D. T. Adroja, F. Ye, H. Cao, G. Sala, M. B. Stone, C. Baines, J. A. T. Verezhak, H. Hu, J.-H. Chung, X. Xu, S.-W. Cheong, M. Nallaiyan, S. Spagna, M. B. Maple, A. H. Nevidomskyy, E. Morosan, G. Chen, and P. Dai, Experimental signatures of a three-dimensional quantum spin liquid in effective spin-1/2  $\text{Ce}_2\text{Zr}_2\text{O}_7$  pyrochlore, *Nature Physics* **15**, 1052 (2019).
- [28] O. Arnold, J. Bilheux, J. Borreguero, A. Buts, S. Campbell, L. Chapon, M. Doucet, N. Draper, R. Ferraz Leal, M. Gigg, V. Lynch, A. Markvardsen, D. Mikkelsen, R. Mikkelsen, R. Miller, K. Palmen, P. Parker, G. Passos, T. Perring, P. Peterson, S. Ren, M. Reuter, A. Savici, J. Taylor, R. Taylor, R. Tolchenov, W. Zhou, and J. Zikovsky, Mantid-Data analysis and visualization package for neutron scattering and  $\mu\text{SR}$  experiments, *Nuclear Instruments and Methods in Physics Research Section A: Accelerators, Spectrometers, Detectors and Associated Equipment* **922**, 166027 (2019).
- [29] O. P. Uzoh, S. Kim, and E. Mun, Influence of crystalline electric field on the magnetic properties of  $\text{CeCd}_3\text{X}_3$  (X = P, As), *Phys. Rev. Materials* **7**, 013402 (2023).



- [30] S. Shin, V. Pomjakushin, L. Keller, P. F. S. Rosa, U. Stuhr, C. Niedermayer, R. Sibille, S. Toth, J. Kim, H. Jang, S.-K. Son, H.-O. Lee, T. Shang, M. Medarde, E. D. Bauer, M. Kenzelmann, and T. Park, Magnetic structure and crystalline electric field effects in the triangular antiferromagnet  $\text{CePtAl}_4\text{Ge}_2$ , *Phys. Rev. B* **101**, 224421 (2020).
- [31] A. Scheie, *PyCrystalField* : software for calculation, analysis and fitting of crystal electric field Hamiltonians, *Journal of Applied Crystallography* **54**, 356 (2021).
- [32] S. Stoll and A. Schweiger, EasySpin, a comprehensive software package for spectral simulation and analysis in EPR, *Journal of Magnetic Resonance* **178**, 42 (2006).
- [33] S. Yunoki and S. Sorella, Two spin liquid phases in the spatially anisotropic triangular Heisenberg model, *Phys. Rev. B* **74**, 014408 (2006).
- [34] D. Yamamoto, G. Marmorini, and I. Danshita, Quantum Phase Diagram of the Triangular-Lattice XXZ Model in a Magnetic Field, *Phys. Rev. Lett.* **112**, 127203 (2014).
- [35] P. A. Maksimov, Z. Zhu, S. R. White, and A. L. Chernyshev, Anisotropic-Exchange Magnets on a Triangular Lattice: Spin Waves, Accidental Degeneracies, and Dual Spin Liquids, *Phys. Rev. X* **9**, 021017 (2019).
- [36] P. Fazekas and P. W. Anderson, On the ground state properties of the anisotropic triangular antiferromagnet, *Philosophical Magazine* **30**, 423 (1974).
- [37] U. Schaffrath and R. Gruehn, Zum chemischen Transport von Verbindungen des Typs  $\text{LnTa}_7\text{O}_{19}$  ( $\text{Ln} = \text{La-Nd}$ ) mit einer Bemerkung zur Strukturverfeinerung von  $\text{NdTa}_7\text{O}_{19}$ , *Zeitschrift für anorganische und allgemeine Chemie* **588**, 43 (1990).
- [38] E. Cavalli, L. Leonyuk, and N. Leonyuk, Flux growth and optical spectra of  $\text{NdTa}_7\text{O}_{19}$  crystals, *Journal of Crystal Growth* **224**, 67 (2001).
- [39] E. Volkova, A. Alekseev, and N. Leonyuk, Crystallization of neodymium heptatantalate from molybdate based flux systems, *Journal of Crystal Growth* **270**, 145 (2004).
- [40] G. C. Guo, J. N. Zhuang, Y. G. Wang, J. T. Chen, H. H. Zhuang, J. S. Huang, and Q. E. Zhang, Dysprosium Tantalum Oxide,  $\text{DyTa}_7\text{O}_{19}$ , *Acta Crystallographica Section C Crystal Structure Communications* **79**, 1000000 (2023).
- [41] J. Sichelschmidt, P. Schlender, B. Schmidt, M. Baenitz, and T. Doert, Electron spin resonance on the spin-1/2 triangular magnet  $\text{NaYbS}_2$ , *Journal of Physics: Condensed Matter* **31**, 205601 (2019).
- [42] F. Grubler, M. Hemmida, S. Bachus, Y. Skourski, H.-A. Krug Von Nidda, P. Gegenwart, and A. A. Tsirlin, Role of alkaline metal in the rare-earth triangular antiferromagnet  $\text{KYbO}_2$ , *Phys. Rev. B* **107**, 224416 (2023).
- [43] W. Zhuo, Z. Zhang, M. Xie, A. Zhang, J. Ji, F. Jin, and Q. Zhang, Magnetism of  $\text{NaYbS}_2$ : From finite temperatures to ground state, *Science China Physics, Mechanics & Astronomy* **67**, 107411 (2024).
- [44] Y. Tokiwa, S. Bachus, K. Kavita, A. Jesche, A. A. Tsirlin, and P. Gegenwart, Frustrated magnet for adiabatic demagnetization cooling to milli-Kelvin temperatures, *Communications Materials* **2**, 42 (2021).